Journal of Materials Chemistry A

Accepted Manuscript

This article can be cited before page numbers have been issued, to do this please use: L. Contreras, S. Ramos-Terrón, A. Riquelme, P. P. Boix, J. A. Idígoras, I. Mora Seró and J. A. Anta, *J. Mater. Chem. A*, 2019, DOI: 10.1039/C9TA02808K.

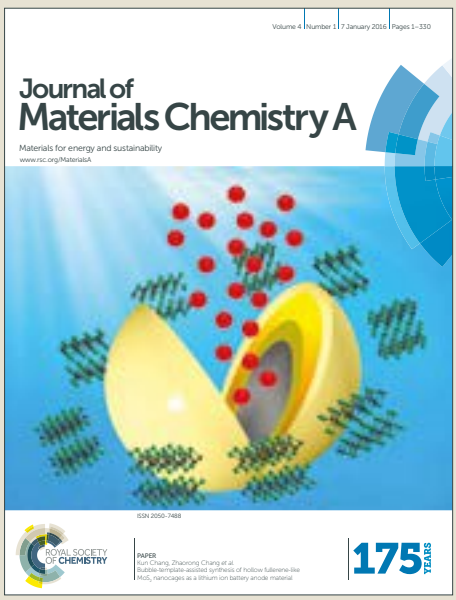

ROYAL SOCIETY OF CHEMISTRY

rsc.li/materials-a

View Article Online
DOI: 10.1039/C9TA02808K

ARTICLE

Impedance analysis of perovskite solar cells: a case study

Received 00th January 20xx,
Accepted 00th January 20xx

DOI: 10.1039/x0xx00000x

Lidia Contreras-Bernal[a,†], Susana Ramos-Terrón[a,†], Antonio Riquelme[a], Pablo Boix[c], Jesús Idígoras[a,*], Iván Mora-Seró [b,*] and Juan A. Anta[a,*]

Metal halide perovskites are mixed electronic-ionic semiconductors with an extraordinary rich optoelectronic behavior and the capability to function very efficiently as active layers in solar cells, with a record efficiency surpassing 23% nowadays. In this work, we carry out an impedance spectroscopy analysis of two perovskite solar cells with quite distinct optical and electrical characteristics, i.e. $MAPbI_3$ and $CsPbBr_3$-based devices. The main aim of the analysis is to establish how, regardless the inherent complexity of the impedance spectrum due to ionic effects, information like ideality factors, recombination losses and the collection efficiency can be qualitative and quantitatively assessed from impedance experiments at operating conditions.

Introduction

Emerging technologies in photovoltaics such as dye-sensitized solar cells, organic solar cells and the more recent concept of halide perovskite solar cells (PSC) have been the object of a huge amount of research in the last few decades.[1,2] These new types of solar cells bring the promise of cheaper synthesis and fabrication processes along with competitive efficiencies. As in any new concept, the state of the art is based on trial-and-error methods and empirical findings. However, a proper understanding of the fundamental processes that take place under operation is still required to further optimize the performance of solar cells. PSCs is a typical "hot" topic example of this due to the impressive progress accomplished in less than ten years, with a current certified record efficiency of 23.7%.[3]

In spite of this progress, some drawbacks and open questions remain. Photovoltaic halide perovskites are ionic compounds with a substantial covalent character and generic structural formula ABX_3, where *A* is an organic or inorganic cation, *B* is the metal center and *X* is a halide. In the most studied perovskite solar cells (those based on $MAPbI_3$: $CH_3NH_3PbI_3$), methylammonium (MA: $CH_3NH_3^+$) is employed as monovalent organic cation, whereas Pb^{2+} and I^- are used as metal and halide, respectively. This material behaves as a sort of "soft" semiconductor where electronic and ionic conduction are mixed.[4,5,6] This feature appears to be related to the occurrence of different kinetic processes that take place in quite separated time scales: electronic transport and recombination in the ns-μs range,[7–9] ionic redistribution and hysteresis in the ms-seconds range,[10–13] and reversible and irreversible degradation processes for seconds, minutes and even in a longer time scale.[14–16] In particular, it is generally accepted that recombination is especially slow and diffusion lengths especially long in PSCs, leading to open-circuit photovoltages very close to the theoretical limits.[7,17–19]

In this context, advanced optoelectronic techniques such as Impedance Spectroscopy (IS)[20,21] are particularly appealing to study solar cells, as they allow the characterization in a broad range of time scales. A typical impedance experiment consists in setting a small frequency-modulated (AC) signal (voltage perturbation) which is applied in addition to a stationary (DC) voltage. By registering the AC response in terms of current one can extract the complex frequency-dependent impedance and obtain information about internal processes of PSC occurring at different time scales (μs – s). This makes it possible to distinguish processes of distinct kinetics, like those based on either pure electronic changes (supposed to be fast) or, indirectly, those based on ionic changes either in the bulk or at interfaces (supposed to be slow). Thus, IS can be theoretically used as characterization method of PSCs and provide a basis to quantify

[a] Área de Química Física, Universidad Pablo de Olavide, Seville, Spain.
[b] Institute of Advanced Materials (INAM), Universitat Jaume I, E-12006 Castelló, Spain
[c] Instituto de Ciencia Molecular, Universidad de Valencia, C/J. Beltrán 2, Paterna, Spain
† Lidia Contreras-Bernal and Susana Ramos-Terrón have equally contributed for the paper.
*Email - anta@upo.es

Electronic Supplementary Information (ESI) available: Scanning electron microscopy images, UV-Vis and EDX spectra, characteristic photovoltaic parameters, Nyquist impedance spectra and impedance-frequency plots under different conditions, electron recombination resistances, HF time constant and collection efficiency versus potential. See DOI: 10.1039/x0xx00000x

View Article Online
DOI: 10.1039/C9TA02808K

transport rates, recombination losses, interfacial charge accumulation processes, characteristic geometric capacitances, ionic diffusion coefficients, etc., occurring in these time domains.

The main drawback of IS, especially as regards its exploitation to characterize PSCs, is that an interpretation of the spectra is still not well-established in the field yet, as it is for other systems such as dye-sensitized solar cells.[21] Several factors contribute to this. First of all, the impedance experiment itself produces internal electrical fields that displace and reorganize the ions, altering the electrical features.[22] Secondly, there is a large variety of equivalent circuits "in the market" to fit the spectra. Due to the existence of the afore-mentioned disparity of kinetics, different types of circuit happen to yield the same fitted parameters.[23] As a consequence, the interpretation of the obtained fitted parameters is not univocally understood yet. Thus, the following questions can be formulated to establish IS as a useful tool to assess the performance of a perovskite solar cell: in spite of the ionic effects and inherent complexity of the spectrum, can we still quantify recombination, and charge collection at working conditions?

Herein, to provide a deeper electrical and phenomenological characterization with new insights in the physical process that determine the photovoltaic response of PSC under working conditions, we have chosen two configurations characterized by very different optical characteristics and band gaps and a quite distinct hysteretic behavior in the current density-voltage curve. In particular, we analyzed the electrical properties of $MAPbI_3$ and $CsPbBr_3$ devices under illumination, being probably the most studied hybrid and inorganic perovskites, respectively. In order to understand the spectra, the impedance parameters (time constants, resistances and capacitances) are analyzed, for both configurations, as a function of three experimental variables: (1) illumination intensity and open-circuit voltage, (2) DC voltage and (3) temperature. From experiment (1) it will be shown how the ideality factor can be extracted, and how it can be qualitatively compared to the recombination rates of PSC with different optical band gaps. From experiment (2) we can follow how the current-voltage curve can be traced down from the impedance response. From experiment (3) we can differentiate between electronic and ionic process and extract activation energies.

With this purpose, perovskite solar cells based on $MAPbI_3$ and $CsPbBr_3$ films were fabricated and characterized. $MAPbI_3$ films were deposited at ambient conditions using a synthesis method where the proportion of PbI_2 and DMSO was adjusted to the environmental relative humidity.[24,25] For $CsPbBr_3$ films, the deposition process was optimized controlling the immersion time, temperature and perovskite solvent to avoid the presence of impurities such as $CsPb_2Br_5$ and Cs_4PbBr_6 in the solution.[26] (see "Experimental section" for details about the fabrication of the films and devices and their characterization by SEM, EDX, UV-Vis and IS). Using these materials as a case study we demonstrate how the recombination loss and the charge collection efficiency can be estimated for cells with different optical band gaps and distinct low frequency behavior, an analysis procedure which is missing so far in the impedance spectroscopy literature.

Results and discussion

After perovskite deposition, pinhole-free and crystalline perovskite layers with close to 400 nm thickness in both cases were formed and characterized for both configurations (Figure S1). As it is well known, the use of different ions affects the morphological (Figure S1A and S2) and optical properties (Figures S1B and S1C).[27 28] Optical band-gaps were extracted from UV-Vis spectra for $MAPbI_3$ (1.61 eV) and $CsPbBr_3$ (2.33 eV), Figure S1C. A relatively long subgap tail is observed in the absorption spectra of $CsPbBr_3$, extending for about 0.6-0.7 eV, in contrast to the tail of only 0.02 eV for $MAPbI_3$ (Figures S1B, S1C).

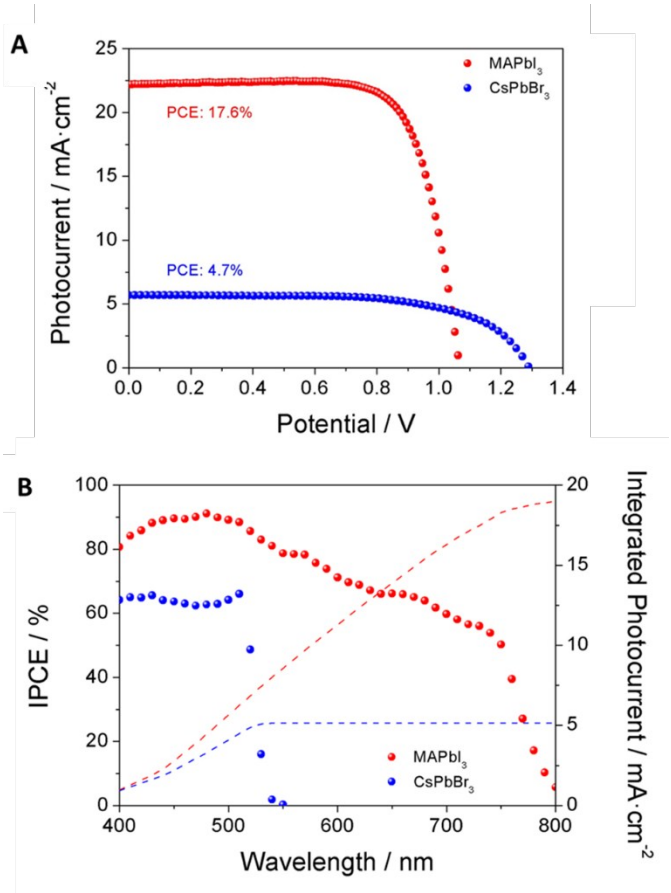

Figure 1. Photovoltaic characterization of $MAPbI_3$ and $CsPbBr_3$ films and solar cells: (A) Density current-voltage characteristic of $MAPbI_3$ and $CsPbBr_3$ based devices in reverse scan under 1 sun – AM 1.5G illumination. A scan rate of 100 $mV{\cdot}s^{-1}$ after poling 20 s at 1.2V and 1.4V was employed for $MAPbI_3$ and $CsPbBr_3$ based devices, respectively. (B) IPCE as a function of monochromatic wavelength and the corresponding AM 1.5G illumination integrated photocurrent.

Figure 1A shows the current-potential (IV) curves obtained for the best performing $MAPbI_3$ and $CsPbBr_3$ devices measured at 1 sun. Statistics of the photovoltaic parameters extracted from all fabricated devices is shown in Figure S3. Average Power Conversion Efficiency (PCE) of 14.9% (short circuit current, J_{SC}: 19.2 $mA{\cdot}cm^{-2}$, Open circuit potential, V_{OC}: 1037 mV and Fill factor, *FF*: 0.74) and

4.1% (J_{SC}: 5.3 mA·cm^{-2}, V_{OC}: 1254 mV and *FF*: 0.61) in a reverse scan of 100 mV/s were obtained for $MAPbI_3$ and $CsPbBr_3$ solar cells respectively. The PCE of $CsPbBr_3$ is substantially lower than the one obtained for $MAPbI_3$. The lower J_{SC} is due, in one hand, to a wider band gap, and on the other, to a lower Incident Photon-to-Electron Conversion Efficiency (IPCE) recorded for $CsPbBr_3$ cell, Figure 1B. The integrated photocurrents are in good agreement with the J_{SC} obtained from IV curve measurements, Figure 1B and S3. After correction by the absorption coefficient, the Internal Quantum Efficiencies (IQE) at stationary conditions has also been measured at 465 and 630 nm and different light intensities. Values very close to 95% are obtained for best $MAPbI_3$ based devices whereas a lower IQE (around 80-90%) is obtained for $CsPbBr_3$ devices.

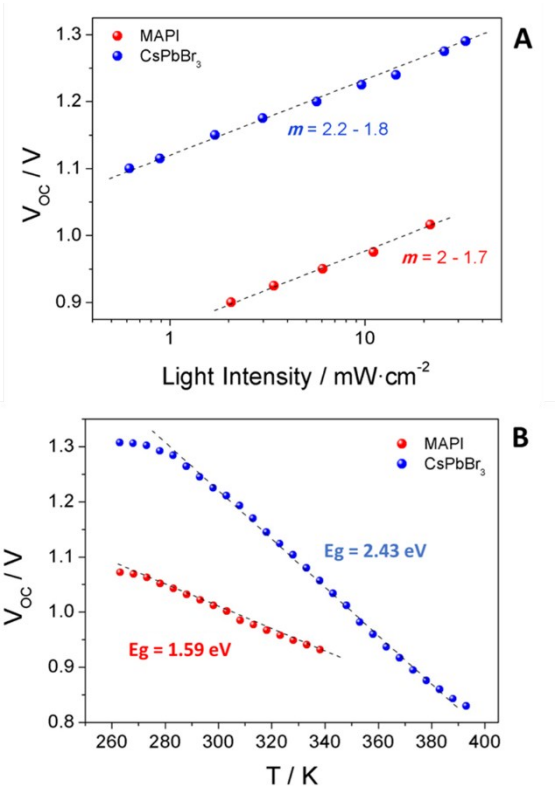

Figure 2. (A) V_{OC} vs. illumination intensity and (B) V_{OC} as a function of the temperature at a light intensity of 14 mW·cm^{-2} using a white-LED as light source. The ideality factors "m" and the estimation of the band gap in accordance to Eq. (5) are shown in panel A and B, respectively.

Figures 2A and 2B show the variation of V_{OC} with respect to illumination intensity and temperature. The V_{OC} has a logarithmic dependence with respect to illumination intensity which follows the diode equation (5), as discussed below. The slope determines the ideality factor (*m*) of the solar cells (Eq. (5)), which lies between 1.7 and 2.2 for both configurations (Figure 2A). The V_{OC} decreases linearly with respect to absolute temperature, except at lower temperatures (Figure 2B). The extrapolation to T → 0 K reproduces the optical band gap of each type of perovskite in good agreement with the optical characterization (Figure S1C).

Both kind of solar devices were characterized by IS. Two types of IS experiments were performed: (1) at open circuit (OC) under varying illumination intensities (results plotted as a function of the resulting V_{OC}) and (2) at non-open-circuit (NOC) conditions varying DC potential (voltage) while light intensity is fixed at 1 sun.[29] In this latter case the parameters are corrected for voltage drop due to the resulting DC current and the corresponding series resistance.[21]

Figure 3 shows representative Nyquist (Z´-Z´´) plots of impedance spectra for both studied configurations under illumination at different photopotentials at OC and different applied potentials at NOC conditions in the 10^6-10^{-2} Hz frequency range. The corresponding Bode plots are depicted in Figure S4. At OC conditions, the Nyquist plots of $MAPbI_3$ based devices (Figure 3A) are characterized by the presence of two arcs and the corresponding frequency plots show two peaks at high and low frequencies accordingly (Figures S4A). The impedance spectra of $CsPbBr_3$ based devices at OC conditions (Figure 3B, S4B) display a different behavior depending on illumination. At very high OC photovoltages (1.3-1.2 V) there are two signals in the high frequency region (10^4-10^6 Hz) that merge into a single one as the V_{OC} is reduced.

Under NOC conditions (Figure 3C and 3D), the Nyquist plots for $MAPbI_3$ and $CsPbBr_3$ based devices were characterized by one complete and well-defined high-frequency arc and, depending on the applied DC potential, a second low frequency arc. The Bode plots display two peaks in the high and frequency regions accordingly, Figures S4C and S4D.

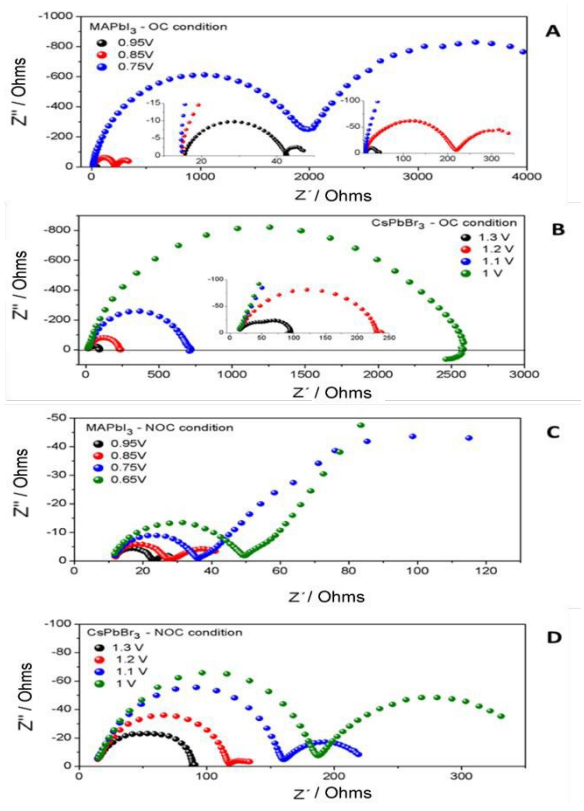

Figure 3. Nyquist plots of impedance spectra obtained under white LED illumination in the vicinity of the 1-sun open-circuit potential for (A, C) $MAPbI_3$

View Article Online DOI: 10.1039/C9TA02808K

and (B, D) $CsPbBr_3$ based devices. In Figures A and B the measurements were carried out under varying illumination and open-circuit (OC) and in Figures C and D the measurement was done at fixed 1-sun equivalent illumination and non-open-circuit (NOC) conditions. Insets: zoom at the high frequency region.

Despite the presence of other minor features, the IS of perovskite solar cells is basically determined by the existence of two characteristic times, at high and low frequencies. Note that the characteristic times can be easily obtained from the reverse of the frequency at which a peak is observed in the Bode plot (Figure S4). The corresponding arc in the Nyquist representation can be described by a parallel association of a resistor and a capacitor, where the time constant is the product of both of them. In order to properly interpret these characteristic times and how a recombination rate or a collection efficiency can be inferred from them, we have performed additional experiments.

On one hand, temperature dependence of IS at short circuit conditions for $MAPbI_3$ based solar cells (i.e. 0 V DC bias in NOC) have been carried out, Figure S5. It can be easily appreciated that the high frequency signal is independent of temperature, *T*. In contrast, the low frequency part varies with *T* and the low frequency signal gets shifted towards higher frequencies when the sample is heated. An activation energy of 36.9 kJ/mol was extracted from these data, Figure S5C, in agreement with previous results.[9,11] This finding suggests that it is in the low frequency region of the spectra where processes that are thermally activated (as could be ionic migrations and/or chemical reactions) are probed, whereas at high frequencies mainly pure electronic processes are determining the response. On the other hand, Figure S6 summarizes the impact of illumination at NOC conditions. We observe that for $MAPbI_3$ based devices, the high frequency time constant shifts towards shorter time scales, whereas the low frequency one remains basically unaltered.

A proper interpretation or analysis of an impedance spectrum requires a suitable model based on rate (continuity) equations. From these equations, an equivalent circuit is derived, which is used to fit the experimental data. However, due to the complexity of the system with electronic and ionic conductivity, there is no broad consensus on the equations ruling perovskite devices. These can include different boundary conditions, such as extracting ones for electrons and blocking ones for ions. On the other hand, the possibility of interfacial reactions cannot be ruled out.[30,31] The lack of a well-stablished model prevents taking full advantage of impedance characterization, which otherwise could allow to extract an important number of parameters. Nevertheless, here we show a semi-empirical approach that allow to extract important parameters. Ideality factors, recombination losses and the collection efficiency can be qualitative and quantitatively assessed at operating conditions.

The recombination rate in units of volume^{-1} and time^{-1} is given by a rate law of the type:[32]

$$U_{rec} \approx -\frac{dn}{dt} = k_T p_0 n^{\gamma} \qquad (1)$$

where *n* is the minority carrier concentration in the active layer (electrons for a p-type semiconductor), p_0 is the majority carrier concentration, k_T is a rate constant and γ is the recombination order. It is possible to relate the carrier concentration with the photopotential and the band gap[32,33]

$$n = (N_C N_V)^{1/x} exp\left(-\frac{E_g - qV}{x k_B T}\right) \qquad (2)$$

where N_c and N_v represent the density of states of the conduction band (CB) and the valence band (VB), respectively. At intrinsic or at high injection conditions, as expected from the inner properties of halide perovskites[34], $n = p$, and the density parameter reduces to $x = 2$. Combining Eqs. (1) and (2) one finds for the recombination current

$$J_{rec} = qdU_{rec} = J_{00} exp\left(-(\gamma/x)\frac{E_g - qV}{k_B T}\right) \qquad (3)$$

where *d* is the thickness of the active layer and J_{00} depends on the rate constant.

Under OC conditions the generation rate of photogenerated carriers *G* should exactly compensate the recombination rate $U_{rec} = G$. Using Eq. (3) the open-circuit photopotential should thus conform to the following equation

$$\frac{J_{00}}{qd} exp\left(-\gamma x \frac{E_g - qV_{OC}}{k_B T}\right) = G \qquad (4)$$

from which one obtains

$$V_{OC} = \frac{E_g}{q} - \frac{m k_B T}{q} ln\left(\frac{J_{00}}{qdG}\right) \qquad (5)$$

where *m*, the ideality factor, is given by $m = x/\gamma$. Equation (5) provides a simple description of the behavior found in Figures 2A and 2B and how the ideality factor and the band gap can be extracted from open-circuit photopotential measurements.

The recombination resistance, R_{rec}, can be defined as the inverse of the voltage derivative of Eq. (3). Consequently, we have

$$R_{rec} = \left(\frac{\partial J_{rec}}{\partial V}\right)^{-1} = R_{00} exp\left(-\frac{\beta q V}{k_B T}\right) \qquad (6)$$

with $R_{00} = (k_B T J_{00}/\alpha q \gamma)\exp(\gamma\alpha E_g/k_B T)$ and $\beta = 1/m$. From this result we also get $m = 1/\beta$. This equation predicts an exponential dependence for the high frequency component of the resistance.

The two features at high frequency (*HF*) and low frequency (*LF*) of the impedance spectra, Figure 3, have been fitted using a simplified equivalent circuit depicted in the inset of Figure 4 B, and the obtained parameters are plotted in Figure 4. This equivalent circuit yields essentially the same results as an alternative one in which the two RC elements (or R-CPE) are placed in series.[23] R_S takes into account the series resistance induced by extracting contacts and wiring. C_{HF} is associated with the geometrical capacitance[35], in line with the

potential independent values obtained and in good agreement with previous works.[23,32,35,36,37] In contrast, the C_{Lf} capacitance shows an exponential trend at high potentials:

$$C_{Lf} = C_{00} exp\left(\frac{\alpha q V}{k_B T}\right) \quad (7)$$

where C_{00} is a preexponential factor and α is a positive parameter. Although the actual choice of the equivalent circuit is not affecting the resistance and capacitance values reported in Fig. 4, a configuration in which the high frequency capacitance is in parallel with the rest of the circuit elements is the choice with the most physical sense in view of the geometrical nature of this capacitance.

Interestingly, the data shows $\alpha = \beta$ (see Table 1) where β is obtained from the slope of the LF resistance, as also reported in the literature.[36,38,39] In addition, the C_{Lf} becomes flat at the same V_d ($V_d = V_{appl}$-V_{series}) at which the resistance reaches its saturation value. These facts point towards a coupled *LF* resistance and capacitance, with a corresponding characteristic time, $\tau_{LF} = R_{LF}C_{LF}$, roughly voltage independent (Figure S7). The complementary behavior of the two circuit elements suggests that the same process that makes the *LF* capacitance to increase with illumination or DC applied voltage makes the *LF* resistance to decrease.

Table 1. β and α parameter values extracted from the high frequency and low frequency resistances and capacitances fitted from impedance spectra for $MAPbI_3$ and $CsPbBr_3$ based devices at open-circuit (OC) and non-open-circuit (NOC) conditions (for NOC conditions only the exponential region is used in the fittings to Eqs. (6) and (7))

Device	IS	β - R_{Hf}	β - R_{Lf}	α - C_{Hf}	α - C_{Lf}
$MAPbI_3$	*OC*	0.56 - 0.5	0.81 - 0.75	flat	0.80 - 0.77
	NOC	0.15 - 0.13	0.51 - 0.46	flat	0.46 - 0.42
$CsPbBr_3$	*OC*	0.51 – 0.43	No signal	flat	No signal
	NOC	0.15 – 0.11	0.46 – 0.40	flat	0.46 – 0.4

Analysis of Figure 4 reveals exponential behavior for both resistances and for the HF capacitance in the high voltage region. The resistances in the OC experiment fit well to Eq. (6). The values of the corresponding slope parameters are collected in Table 1.

R_{Hf} obtained for $MAPbI_3$ and $CsPbBr_3$ -based devices show a similar β parameter value at OC conditions, of around 0.5. This follows the expected dependence for a dominating recombination resistance, R_{rec}, considering the ideality factor measured in Figure 2A. In contrast, values around 0.78 were found for the R_{Lf} of $MAPbI_3$ devices at OC. It is worth mentioning the different voltage-dependence for the *LF* and *HF* resistances, which is not the case reported in previous works.[9,36] Considering the different nature of the low and high frequency signals described above, this behavior is not unexpected.

At NOC conditions the behavior of the two resistances is quite different. Firstly, the exponential dependence is only observed at high DC potentials but becomes flat as the experiment approaches SC conditions, which suggests that the device is ruled by the shunt resistance at fixed light intensity and low applied bias. The transition between the two regimes occurs at voltages right below the maximum power point of the corresponding IV curves (Figure 1A).

Secondly, at high applied bias in NOC the slope in good agreement with the ideality factor is that at *LF*. Note that in Figure 4 NOC parameters are plotted as a function of the device potential, $V_d = V_{appl}$-V_{series}, where the applied voltage, V_{appl}, is corrected by the subtraction of the voltage drop at the series resistance, V_{series}. It is important to stress out that the series resistance correction does not change significantly the slope of neither the two resistances (Figure S8)

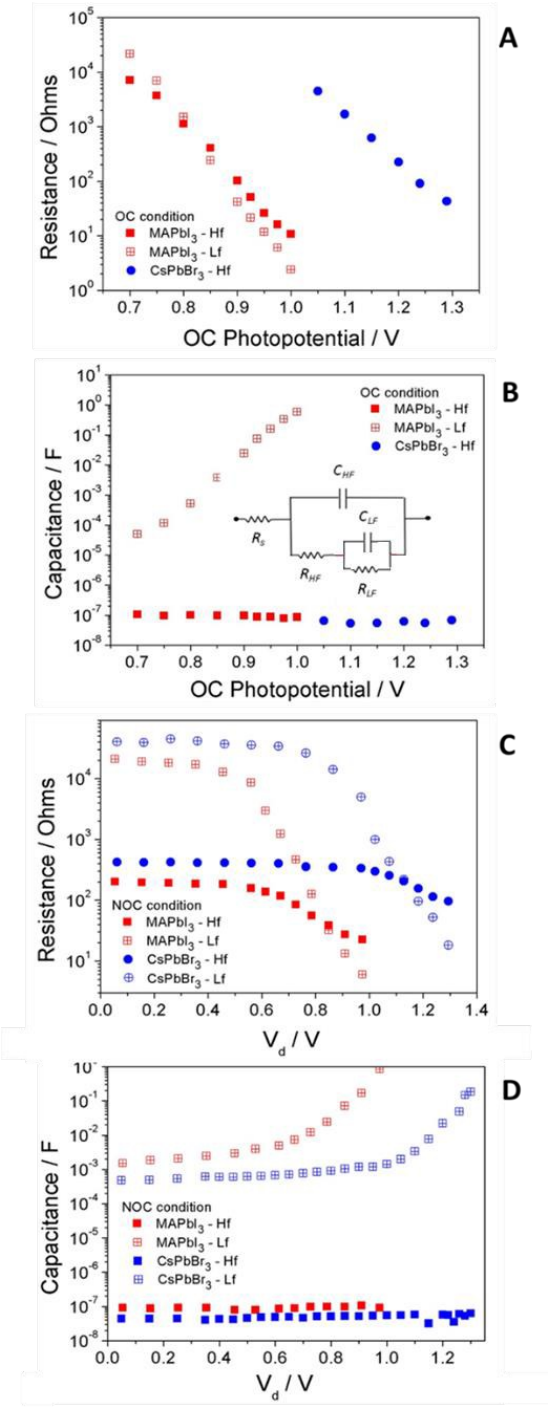

Figure 4. (A, B) Resistive and (C, D) capacitance elements as extracted from fittings of the impedance spectra obtained at (A, B) open-circuit (OC) and (C, D) non-open-circuits (NOC) conditions using the equivalent circuit model for

View Article Online
DOI: 10.1039/C9TA02808K

(red) $MAPbI_3$ and (blue) $CsPbBr_3$ based devices. At NOC conditions, parameters are plot versus the series corrected potential $V_d = V_{appl}-V_{series}$

As previously discussed, there is not consensus on the interpretation of the elements producing the low frequency arc, but all the models point that ionic movement is related to the origin of this feature. This lack of consensus is mainly due to the difficulty of interpretation of the physical origin of each one of the parameters of the equivalent circuit. While, in dye sensitized solar cell just one physical process can be assigned to each parameter in the case of PSCs, different processes present similar characteristic times and it is difficult to decouple their effect. Consequently, different processes affect the same feature. For example, *HF* arc has been previously ascribed to account for R_{rec}[32] but it is also affected by selective contact or perovskite transport.[35,40,41] In the same, line, R_{rec} has been related with the *LF* arc[40] or with both[6,9,39,42], as it is not straightforward to decouple the recombination contribution from other contributions, as transport or injection at the interfaces

Since at OC the R_{Hf} slope is in good agreement with the ideality factor, indicating that this resistance is linearly proportional to R_{rec} as expected from Eqs. (5) and (6), the results are consistent with intrinsic or high injection (x = 2) conditions and a recombination reaction order of $\gamma \sim 1$, a signature of Shockley-Read-Hall (SRH) recombination for both $MAPbI_3$ and $CsPbBr_3$.[32,43] Eq. (5) also predicts a linear dependence of V_{OC} versus absolute temperature. This behavior is indeed reproduced in Figure 2B and the fact that the optical band gap is recovered by extrapolation to $T \rightarrow 0$ K, strongly suggests that, at least under OC conditions, the recombination process represented by the rate law (Eq. 1) takes place in the bulk or it is determined by the perovskite layer only. This is consistent with previous findings using ideality factor[43], different optical penetrations of the light in impedance experiments with different excitation wavelengths,[44,32] and the comparison of devices made with alternative contact layers.[45–47]

The exponential dependence of R_{Hf} with voltage and its proportional connection to R_{rec} at OC allows for a direct comparison between $MAPbI_3$ and $CsPbBr_3$ recombination behaviors. To do that, it is necessary to take into account both the thermodynamic effect (different band gap) and the kinetic behavior (recombination rate), plotting the impedance parameters at the same value of the photogenerated charge density. Eq. (2) provides a means to do this. According to this expression, plotting versus $E_g/q - V_{oc}$ makes sure that we are comparing cells of different band gaps at the same value of the photogenerated charge density. The correction is analogous to an analysis commonly done in dye-sensitized solar cells,[48,49] and would be valid if the $n = p$ condition is fulfilled, i.e., at intrinsic or at high injection conditions.

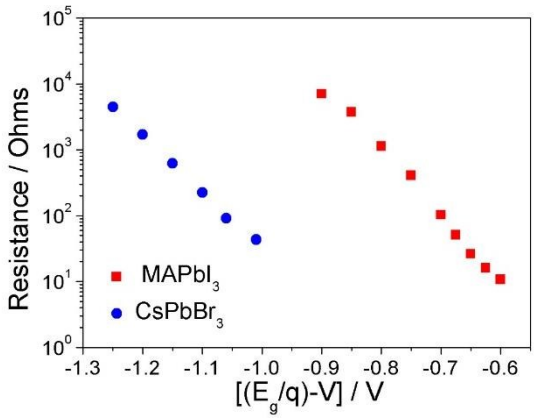

Figure 5. High frequency resistances at OC conditions corrected for the optical band gap of each perovskite.

Once the effect of the band gap is corrected for (Figure 5), it becomes evident that the recombination rate in $CsPbBr_3$ based devices is substantially larger than in the $MAPbI_3$ ones. This could be expected from the potential loss with respect to the band gaps, which is ~1 V for $CsPbBr_3$ ($E_g/q - V_{OC}$ = 2.34 – 1.3) versus ~0.45 V for $MAPbI_3$ ($E_g/q - V_{OC}$ = 1.55 – 1.1). The difference roughly coincides with the voltage separation between the two resistances in Figure 5.

At NOC and high applied voltage, it is R_{Lf} the one than presents a slope concurring with the ideality factor, and consequently, proportional to R_{rec}. Thus, the same correction of thermodynamic effect can be applied with similar results than those in Figure 5 (Figure S9).

The faster recombination in $CsPbBr_3$ devices, which is derived from the analysis, is most probably related to their rougher morphology and longer tail of subgap states observed in the absorption spectra (Figure S1). A relatively long *Urbach* tail will lead to a substantial V_{oc} loss with respect to the thermodynamic limit.[19] In addition, more crystal defects will cause a more rapid recombination rate, that may cause additional voltage loss. Thus, recombination is of the same type as in $MAPbI_3$ cells, as indicated by a similar value of the ideality factor, but it is faster due to a higher concentration of defects (parameter p_0 in Eq (1)). In a recent publication, a 300-400 mV voltage loss in bromine-based devices is attributed to surface recombination.[50] However, contrary to our results, the reported activation energy at $T \rightarrow 0$ is significantly lower than the optical band gap, and the authors do not detect any Urbach tail in their IPCE measurements, showing that in their case the main voltage loss arises from band misalignment and recombination mediated by interfacial effects. Consequently, the T analysis allows discriminating between surface and bulk recombination, while impedance comparison permits comparing the recombination rate when the thermodynamic effect is corrected for, as in Figure 5.

As mentioned in the introduction, the main objective of this work is to establish an approach to quantify recombination losses and charge collection from the impedance spectrum. First of all, it is

View Article Online
DOI: 10.1039/C9TA02808K

important to verify that the two resistances at NOC and steady-state conditions, can be used to reconstruct the IV curve[21,29,42], taking into account all contributions related with recombination, transport, injection or series resistance:

$$J(V) = J_{SC} - A\int_0^{V_{app}} \frac{dV}{R_{tot}} \quad (8)$$

with $R_{tot} = R_s + R_{HF} + R_{LF}$ (A is the active area of the device). In Figure S10 it is shown that the experimental curves for both $MAPbI_3$ and $CsPbBr_3$ based devices can be recovered, using Eq. (8), from the impedance data at NOC conditions.

Following previous work[42], the charge collection efficiency, CCE, in a solar cell can be determined from the recombination resistance at OC and NOC conditions using the expression:

$$CCE \approx 1 - \frac{R_{rec(OC)}}{R_{rec(NOC)}} \quad (9)$$

where R_{rec} is the recombination resistance as defined by Eq. (6). Hence, at open-circuit CCE = 0 by definition and at short-circuit, for an optimal system with minimum recombination, R_{rec} (V = 0) → ∞ and CCE → 1.

The main challenge, thus, is how to define and extract R_{rec} from the impedance spectrum. As outlined before, several possibilities have been proposed in the literature. Since no definitive theoretical model for impedance is well-established yet, we apply here an *empirical* approach. In the studied devices, the OC high frequency resistance is the feature which follows the same voltage dependence as the ideality factor, in line with Eqs. (5) and (6). However, at NOC conditions it is the low frequency resistance the one with a slope closer to the ideality factor. Thus, in order to identify the recombination resistance, it is necessary to independently evaluate high and low frequency resistances, as well as the sum of the two. All three possibilities are tested in Figure S11 in Supporting Information. Due to the fact that $R_{LF} >> R_{HF}$ (see Figure 4C) at NOC conditions, only assuming $R_{rec} \approx R_{HF}$ yields values significantly different from 100%. As a matter of fact, only this possibility makes it possible to *discriminate* between $MAPbI_3$ and $CsPbBr_3$ cells, as observed in Figure 6.

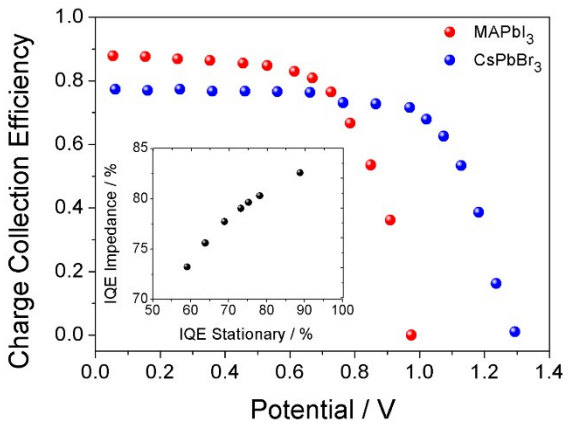

Figure 6. Charge collection efficiency as predicted from Eq. (9) if the R_{rec} is temptatively assumed to be equal to R_{HF}. Inset: comparison between the prediction of Eq. (9) at short-circuit with $R_{rec} \approx R_{HF}$ and the stationary value of the IQE for a batch of MAPbI3 devices.

The collection efficiency of photogenerated electrons in the perovskite film can be considered an approximation to the IQE (assuming that there are no charge losses in the injection of chargers to the contacts). The variation of the collection efficiency in Figure 6 with DC potential resembles the shape of the JV curve. The curve yields the collection efficiency at SC conditions (V = 0). Values of ~ 0.9 and ~ 0.8 are obtained for $MAPbI_3$ and $CsPbBr_3$ based devices, respectively. These figures agree remarkably well with IQE values measured for both configurations, which confirms the larger recombination loss for $CsPbBr_3$ cells.

Additional evidence that there is a substantial recombination loss in $CsPbBr_3$ devices, even at SC conditions, is provided by the maximum theoretical photocurrents, as obtained from integration of the measured absorptance (Figure S12). Values of 24.9 and 10.8 mA/cm^2 are obtained for $MAPbI_3$ and $CsPbBr_3$ based devices, respectively. When compared with the actual experimental values, 20 ± 2 and 5 ± 1 mA/cm^2, we infer that recombination losses (and possibly poorer injection too) are affecting critically the performance of the devices made with $CsPbBr_3$ perovskite.

The prediction of the collection efficiencies evidences that the impedance response changes from a regime where recombination is dominant: $V > V_{mp}$, and both resistances show an exponential behavior (although with different slopes), and a regime where collection is dominant: $V < V_{mp}$ and both resistances become flat. As the recombination resistance increases exponentially as the voltage decreases, at low voltages the impedance response becomes determined by the other elements in the equivalent circuit like shunting and transport resistances, which are effectively voltage independent. The previous results in terms of ideality factors and CCE point to a phenomenological determination of CCE using the high frequency component as the impedance element that basically contains the information about recombination losses. However, the exponential behavior of R_{LF} at NOC conditions implies that this identification is not so straightforward. To provide additional assurance we have measured the IQE at short-circuit of a batch of $MAPbI_3$ based devices and plotted the results versus the predictions of Eq. (9) at V = 0 using $R_{rec} \approx R_{HF}$ in Eq. (9) for the determination of IQE. In this respect, we have to bear in mind that CCE and IQE, although related, do not represent exactly the same thing and they can only be identified if there are not additional losses between photocarrier generation and carrier collection (like for instance poor injection of excitation dissociation).

The results in the inset of Figure 6 reveal a clear correlation between both magnitudes. This demonstrates that the impedance of the high frequency signal provides a phenomenological way to evaluate IQE. However, impedance values do not exactly coincide with IQE stationary measurements, being the difference larger the less efficient a particular cell is. For instance, for the most efficient specimen of the batch the prediction of Eq. (9) is ~0.83, whereas the stationary measurement gives ~0.88. Assuming that there are no additional losses after photocarrier generation, this difference

View Article Online
DOI: 10.1039/C9TA02608K

means that the R_{HF} cannot be naïvely identified with the recombination resistance and probably includes other contributions as transport, interfacial and ion-mediated dielectric relaxation mechanisms.[51]

Conclusions

$MAPbI_3$ and $CsPbBr_3$ perovskite solar cells have been thoroughly studied by impedance spectroscopy at open-circuit and non-open-circuit conditions, at different illuminations and temperatures. Despite the difficulty of decoupling the different processes occurring in the photovoltaic device, a resistance linearly related with recombination resistance can be obtained by comparing the exponential slope with the ideality factor. We have shown that these resistances can be used to extract information, both qualitative and semi-quantitative, about the nature of recombination. Correction is needed if cells of different band gaps are compared. The use of this protocol allowed us to establish, as a case study, that $MAPbI_3$ and $CsPbBr_3$ perovskite solar cells analyzed in this work have the same recombination mechanism (trap-limited in the bulk) but it is much faster in $CsPbBr_3$ devices, possibly due to a larger concentration of subgap states.

High-frequency resistances measured at OC and NOC conditions are found to provide an estimation of the charge collection efficiency along the JV curve. However, both low and high frequency resistances probably include additional mechanisms such as transport and dielectric contributions. Further efforts are therefore required to develop a robust model to describe the impedance response of perovskite solar cells.

Experimental Section

Fabrication of the perovskite solar cell devices

Perovskite solar devices were fabricated on FTO-coated glass (Pilkington–TEC15) patterned by laser etching. Before the deposition, the substrates were cleaned using Hellmanex® solution and rinsed with deionized water and ethanol. Thereupon, they were ultrasonicated in 2-propanol and dried by using compressed air. The TiO_2 blocking layer was deposited onto the substrates by spray pyrolysis at 450 °C, using a titanium diisopropoxide bis(acetylacetonate) solution (75% in 2-propanol, Sigma Aldrich) diluted in ethanol (1:14, v/v), with oxygen as carrier gas. The TiO_2 compact layer was then kept at 450 °C for 30 min for the formation of anatase phase. Once the samples achieve room temperature, a TiO_2 mesoporous layer was deposited by spin coating at 2000 rpm during 10 s using a commercial TiO_2 paste (Dyesol, 18NR-T) diluted in ethanol (1:5, weight ratio). After drying at 100 °C for 10 min, the TiO_2 mesoporous layer was heated at 500 °C for 30 min and later cooled to room temperature. An additional doping treatment using Li^+ ions (10.04 mg LiTFSI in 1 ml acetonitrile, 35mM) was used for the TiO_2 mesoporous layer prior to $CsPbBr_3$ deposition.

For $MAPbI_3$ based devices, a pure methylammonium lead iodide solution were prepared to be deposited by spin coating using a methodology previously reported:[24,25] The perovskite precursor solution was adjusted to the relative humidity of the environment (42% R.H.) by the Pb/DMSO ratio. The perovskite precursor solution (50 µL) was spin-coated in a one-step setup at 4000 rpm for 50 s. During this step, DMF is selectively washed with non-polar diethyl ether just before the white solid begins to crystallize in the substrate. For $CsPbBr_3$ based devices a two-step sequential deposition technique was employed. Firstly, a dissolution of $PbBr_2$ in DMF (1M) was prepared by heating at 75 °C for 20 min and filtered (pore size 0.45µm). This solution was spin-coated (2500 rpm – 30 s) on TiO_2 mesoporous film. During the deposition process, the dissolution was kept at 75 °C. Afterward, the substrate was dried on a hot plate at 70 °C for 30 min. Subsequently, the substrates were dipped for 10 min in a solution of 17 mg/mL CsBr in methanol at 60 °C. Then, the substrates were annealed at 250 °C for 10 min.

For the both $MAPbI_3$ and $CsPbBr_3$ based devices, Spiro-OMeTAD was deposited as hole selective material by dissolving 72.3 mg in 1 mL of chlorobenzene as well as 17.5 µL of a lithium bis (trifluoromethylsulphonyl)imide (LiTFSI) stock solution (520 mg of LiTFSI in 1mL of acetonitrile), and 28.8 µL of 4-tert-butylpyridine (TBP). The Spiro-OMeTAD was spin coated at 4000 rpm for 30 s. The solution was filtered with a 0.2 µm PTFE filter prior to their deposition. Finally, 60 nm of gold was deposited as a metallic contact by thermal evaporation under a vacuum level between $1{\cdot}10^{-6}$ and $1{\cdot}10^{-5}$ torr. All the deposition processes were carried out outside a glovebox under environmental conditions.

Characterization of the devices

Current-voltage characteristics of the devices were obtained using a solar simulator (ABET-Sun2000) under 100mW/cm^2 illumination with AM 1.5G filter. The light intensity was recorded using a reference mono-crystalline silicon solar cell with temperature output (ORIEL, 91150). A metal mask was used to define an active area of 0.16 cm^2. The current-voltage characteristics were determined by applying an external potential bias to the cell and measuring the photocurrent using an Autolab/PGSTAT302N potentiostat. The current-voltage characteristics were measured with a scan rate of 100 mV/s and a sweep delay of 20s. Incident Photon-to-current Conversion efficiency (IPCE) was measured using an Oriel Xenon lamp coupled to McPherson monochromator. Light intensity was determined as a function of the wavelength using a calibrated silicon photodiode (PH-100 Si, GENTECE).

The illumination for the IS measurements was provided by white LED over a wide range of DC light intensities. Two types of IS experiments were performed: (1) at open circuit (OC) under varying illumination intensities (parameters are extracted, analyzed and plotted as a function of the resulting open-circuit photopotential) and (2) at non open circuit (NOC) conditions varying DC potential (voltage) while light intensity is fixed.[29] In this latter case the parameters are corrected for voltage drop due to the resulting DC current and the corresponding series resistance.[21] In the following, we will use the labels OC and NOC to refer to these two kinds of experiments. In both OC and NOC conditions a 20 mV perturbation in the 10^6-10^{-2} Hz range was applied. A response analyzer module (PGSTAT302N/FRA2, Autolab) was utilized to analyze the frequency response of the devices.

IMPS measurements were carried out by coupling the PGSTAT302N/FRA2 module to the LED. IMPS measurements were performed at short-circuit with a light perturbation corresponding to 10% of the DC background illumination intensity. Due to limitations of the experimental set-up, the measurement was limited to the 10^5 - 10^{-1}Hz frequency range. The NOVA 1.7 software was used to generate data. Z-view equivalent circuit modelling software (Scribner) was used to fit the spectra.

For the structural characterization, Scanning Electron Microscope (SEM) images of the samples were performed using a Zeiss GeminiSEM-300 microscope working at 2KeV. Energy Dispersive Spectroscopy (EDS) was performed using a Silicon Drift Detector (Oxford Instruments). For optical characterization, UV-Visible absorption spectra were recorded by using a Cary 100 UV-Vis spectrophotometer (Agilent) in the range of 400-800 nm. Steady state photoluminescence measurements were performed using a Hitachi, F-7000 Fluorescence spectrophotometer. Temperature-dependent experiments were carried out by means of a MHCS622CD Heating and Cooling Vacuum/gas tight Stage configured with MTDC600 temperature controller (Microptik).

Conflicts of interest

The authors declare no competing financial interest.

Acknowledgements

We thank Junta de Andalucía for financial support via grant FQM 1851 and FQM 2310. We thank Ministerio de Economía y Competitividad of Spain and Agencia Estatal de Investigación (AEI) and EU (FEDER) under grants MAT2013-47192-C3-3-R, MAT2016-76892-C3-2-R, MAT2016-79866-R and Red de Excelencia "Emerging photovoltaic Technologies" for financial support. We also thank Servicio de Microscopía Electrónica (Universidad Pablo de Olavide). I.M.S. thanks the European Research Council (ERC) via Consolidator Grant (724424 - No-LIMIT). P.P. B thank the MINECO for his RyC contract and MAT2017-88821-R, and acknowledges the financial support from the Conselleria d'Educació, Investigació, Cultura i Esport Valenciana (SEJI2017/2017/012).

Notes and references

1 H. J. Snaith, *J. Phys. Chem. Lett.*, 2013, **4**, 3623–3630.
2 S. Karazhanov and V. Kharton, *Mater. Lett.*, 2018, **228**, 450.
3 NREL, NREL: National Center for Photovoltaics Home Page, http://www.nrel.gov/ncpv/, (accessed 5 March 2015).
4 C. Eames, J. M. Frost, P. R. F. Barnes, B. C. O'Regan, A. Walsh and M. S. Islam, *Nat. Commun.*, DOI:10.1038/ncomms8497.
5 R. A. Kerner and B. P. Rand, *J. Phys. Chem. Lett.*, 2018, **9**, 132–137.
6 D. Moia, I. Gelmetti, P. Calado, W. Fisher, M. Stringer, O. Game, Y. Hu, P. Docampo, D. Lidzey, E. Palomares, J. Nelson and P. R. F. Barnes, *ArXiv180506446 Cond-Mat Physicsphysics*.
7 G. Xing, N. Mathews, S. Sun, S. S. Lim, Y. M. Lam, M. Grätzel, S. Mhaisalkar and T. C. Sum, *Science*, 2013, **342**, 344–347.
8 S. D. Stranks, V. M. Burlakov, T. Leijtens, J. M. Ball, A. Goriely and H. J. Snaith, *Phys. Rev. Appl.*, 2014, **2**, 034007.
9 A. Pockett, G. E. Eperon, N. Sakai, H. J. Snaith, L. M. Peter and P. J. Cameron, *Phys. Chem. Chem. Phys.*, 2017, **19**, 5959–5970.
10 C. Li, S. Tscheuschner, F. Paulus, P. E. Hopkinson, J. Kießling, A. Köhler, Y. Vaynzof and S. Huettner, *Adv. Mater.*, 2016, **28**, 2446–2454.
11 L. Contreras, J. Idígoras, A. Todinova, M. Salado, S. Kazim, S. Ahmad and J. A. Anta, *Phys. Chem. Chem. Phys.*, 2016, **18**, 31033–31042.
12 G. Richardson, S. E. J. O'Kane, R. G. Niemann, T. A. Peltola, J. M. Foster, P. J. Cameron and A. B. Walker, *Energy Environ. Sci.*, 2016, **9**, 1476–1485.
13 H. J. Snaith, A. Abate, J. M. Ball, G. E. Eperon, T. Leijtens, N. K. Noel, S. D. Stranks, J. T.-W. Wang, K. Wojciechowski and W. Zhang, *J. Phys. Chem. Lett.*, 2014, **5**, 1511–1515.
14 G. Niu, X. Guo and L. Wang, *J. Mater. Chem. A*, 2014, **3**, 8970–8980.
15 K. Domanski, B. Roose, T. Matsui, M. Saliba, S.-H. Turren-Cruz, J.-P. Correa-Baena, C. R. Carmona, G. Richardson, J. M. Foster, F. D. Angelis, J. M. Ball, A. Petrozza, N. Mine, M. K. Nazeeruddin, W. Tress, M. Grätzel, U. Steiner, A. Hagfeldt and A. Abate, *Energy Environ. Sci.*, 2017, **10**, 604–613.
16 M. Bag, L. A. Renna, R. Y. Adhikari, S. Karak, F. Liu, P. M. Lahti, T. P. Russell, M. T. Tuominen and D. Venkataraman, *J. Am. Chem. Soc.*, 2015, **137**, 13130–13137.
17 S. D. Stranks, G. E. Eperon, G. Grancini, C. Menelaou, M. J. P. Alcocer, T. Leijtens, L. M. Herz, A. Petrozza and H. J. Snaith, *Science*, 2013, **342**, 341–344.
18 J. S. Manser, J. A. Christians and P. V. Kamat, *Chem. Rev.*, DOI:10.1021/acs.chemrev.6b00136.
19 W. Tress, *Adv. Energy Mater.*, 2017, **7**, 1602358.
20 E. Barsoukov and J. R. Macdonald, Eds., *Impedance Spectroscopy: Theory, Experiment, and Applications*, Wiley-Interscience, Hoboken, N.J, 2 edition, 2005.
21 F. Fabregat-Santiago, G. Garcia-Belmonte, I. Mora-Seró and J. Bisquert, *Phys. Chem. Chem. Phys.*, 2011, **13**, 9083–9118.
22 D. Pitarch-Tena, T. T. Ngo, M. Vallés-Pelarda, T. Pauporté and I. Mora-Seró, *ACS Energy Lett.*, 2018, **3**, 1044–1048.
23 A. Todinova, L. Contreras-Bernal, M. Salado, S. Ahmad, N. Morillo, J. Idígoras and J. A. Anta, *ChemElectroChem*, DOI:10.1002/celc.201700498.
24 C. Aranda, C. Cristobal, L. Shooshtari, C. Li, S. Huettner and A. Guerrero, *Sustain. Energy Fuels*, 2017, **1**, 540–547.
25 L. Contreras-Bernal, C. Aranda, M. Valles-Pelarda, T. T. Ngo, S. Ramos-Terrón, J. J. Gallardo, J. Navas, A. Guerrero, I. Mora-Seró, J. Idígoras and J. A. Anta, *J. Phys. Chem. C*, DOI:10.1021/acs.jpcc.8b01558.
26 X. Zhang, W. Wang, B. Xu, S. Liu, H. Dai, D. Bian, S. Chen, K. Wang and X. W. Sun, *Nano Energy*, 2017, **37**, 40–45.
27 E. T. Hoke, D. J. Slotcavage, E. R. Dohner, A. R. Bowring, H. I. Karunadasa and M. D. McGehee, *Chem. Sci.*, 2015, **6**, 613–617.
28 G. E. Eperon, S. D. Stranks, C. Menelaou, M. B. Johnston, L. M. Herz and H. J. Snaith, *Energy Environ. Sci.*, 2014, **7**, 982–988.

29 F. Fabregat-Santiago, M. Kulbak, A. Zohar, M. Vallés-Pelarda, G. Hodes, D. Cahen and I. Mora-Seró, *ACS Energy Lett.*, 2017, **2**, 2007–2013.

30 A. Guerrero, J. You, C. Aranda, Y. S. Kang, G. Garcia-Belmonte, H. Zhou, J. Bisquert and Y. Yang, *ACS Nano*, DOI:10.1021/acsnano.5b03687.

31 M. D. Bastiani, G. Dell'Erba, M. Gandini, V. D'Innocenzo, S. Neutzner, A. R. S. Kandada, G. Grancini, M. Binda, M. Prato, J. M. Ball, M. Caironi and A. Petrozza, *Adv. Energy Mater.*, 2016, **6**, 1501453.

32 L. Contreras-Bernal, M. Salado, A. Todinova, L. Calio, S. Ahmad, J. Idígoras and J. A. Anta, *J. Phys. Chem. C*, 2017, **121**, 9705–9713.

33 S. M. Sze and K. K. Ng, *Physics of Semiconductor Devices*, John Wiley & Sons, 2006.

34 Y. Chen, H. T. Yi, X. Wu, R. Haroldson, Y. N. Gartstein, Y. I. Rodionov, K. S. Tikhonov, A. Zakhidov, X.-Y. Zhu and V. Podzorov, *Nat. Commun.*, 2016, **7**, 12253.

35 A. Guerrero, G. Garcia-Belmonte, I. Mora-Sero, J. Bisquert, Y. S. Kang, T. J. Jacobsson, J.-P. Correa-Baena and A. Hagfeldt, *J. Phys. Chem. C*, 2016, **120**, 8023–8032.

36 I. Zarazua, G. Han, P. P. Boix, S. Mhaisalkar, F. Fabregat-Santiago, I. Mora-Seró, J. Bisquert and G. Garcia-Belmonte, *J. Phys. Chem. Lett.*, 2016, **7**, 5105–5113.

37 A. Pockett, G. E. Eperon, T. Peltola, H. J. Snaith, A. Walker, L. M. Peter and P. J. Cameron, *J. Phys. Chem. C*, 2015, **119**, 3456–3465.

38 I. Zarazua, J. Bisquert and G. Garcia-Belmonte, *J. Phys. Chem. Lett.*, 2016, 525–528.

39 Z. Zolfaghari, E. Hassanabadi, D. Pitarch-Tena, S. J. Yoon, Z. Shariatinia, J. van de Lagemaat, J. M. Luther and I. Mora-Seró, *ACS Energy Lett.*, 2019, **4**, 251–258.

40 E. J. Juarez-Perez, M. Wuβler, F. Fabregat-Santiago, K. Lakus-Wollny, E. Mankel, T. Mayer, W. Jaegermann and I. Mora-Sero, *J. Phys. Chem. Lett.*, 2014, **5**, 680–685.

41 M. Anaya, W. Zhang, B. C. Hames, Y. Li, F. Fabregat-Santiago, M. E. Calvo, H. J. Snaith, H. Míguez and I. Mora-Seró, *J. Mater. Chem. C*, 2017, **5**, 634–644.

42 I. Zarazúa, S. Sidhik, T. Lopéz-Luke, D. Esparza, E. De la Rosa, J. Reyes-Gomez, I. Mora-Seró and G. Garcia-Belmonte, *J. Phys. Chem. Lett.*, 2017, 6073–6079.

43 W. Tress, M. Yavari, K. Domanski, P. Yadav, B. Niesen, J. P. C. Baena, A. Hagfeldt and M. Graetzel, *Energy Environ. Sci.*, 2018, **11**, 155–165.

44 D. Bi, W. Tress, M. I. Dar, P. Gao, J. Luo, C. Renevier, K. Schenk, A. Abate, F. Giordano, J.-P. C. Baena, J.-D. Decoppet, S. M. Zakeeruddin, M. K. Nazeeruddin, M. Grätzel and A. Hagfeldt, *Sci. Adv.*, 2016, **2**, e1501170.

45 J. Idígoras, L. Contreras-Bernal, J. M. Cave, N. E. Courtier, Á. Barranco, A. Borras, J. R. Sánchez-Valencia, J. A. Anta and A. B. Walker, *Adv. Mater. Interfaces*, 2018, **5**, 1801076.

46 S. Ravishankar, S. Gharibzadeh, C. Roldán-Carmona, G. Grancini, Y. Lee, M. Ralaiarisoa, A. M. Asiri, N. Koch, J. Bisquert and M. K. Nazeeruddin, *Joule*, 2018, **2**, 788–798.

47 K. Valadez-Villalobos, J. Idígoras, L. P. Delgado, D. Meneses-Rodríguez, J. A. Anta and G. Oskam, *J. Phys. Chem. Lett.*, 2019, **10**, 877–882.

48 S. R. Raga, E. M. Barea and F. Fabregat-Santiago, *J. Phys. Chem. Lett.*, 2012, **3**, 1629–1634.

49 J. Idígoras, L. Pellejà, E. Palomares and J. A. Anta, *J. Phys. Chem. C*, 2014, **118**, 3878–3889.

50 A. Zohar, M. Kulbak, I. Levine, G. Hodes, A. Kahn and D. Cahen, *ACS Energy Lett.*, 2018, 1–7.

51 J. Bisquert, L. Bertoluzzi, I. Mora-Sero and G. Garcia-Belmonte, *J. Phys. Chem. C*, 2014, **118**, 18983–18991.

View Article Online DOI: 10.1039/C9TA02808K